

Research on damage of solid-web steel reinforced concrete T-shaped columns subjected to various loadings

Jiayang Xue^{*}, Chaofeng Zhou^a and Zuqiang Liu^b

College of Civil Engineering, Xi'an University of Architecture and Technology, Xi'an, China

(Received November 09, 2016, Revised March 13, 2017, Accepted April 18, 2017)

Abstract. This paper presents an experimental study on damage evolution laws of solid-web steel reinforced concrete (SRC) T-shaped columns along the direction of the web under various loadings. Ten specimens with a scale ratio of 1/2 and a shear span ratio of 2.5 were designed and fabricated. The influences of various parameters, including the axial compression ratio, steel ratio, and loading mode, were examined. The mechanical performances including load-displacement curve and energy dissipation capacity under the monotonic and low cyclic loadings were analyzed. Compared with the monotonic loading, bearing capacity, ultimate deformation capacity, and energy dissipation capacity of the specimens decrease to some extent with the increase of the displacement amplitude and the number of loading cycle. The results show that the damage process of the SRC T-shaped column can be divided into five stages, namely non-damage, slight-damage, steadily-developing-damage, severe-damage and complete-damage. Finally, based on the Park-Ang model, a modified nonlinear damage model which combines the maximum deformation with hysteretic energy dissipation is proposed by taking into account the dynamic influence of the aforementioned parameters. The results show that the modified model in this paper is more accurate than Park-Ang model and can better describe the damage evolution of SRC T-shaped columns.

Keywords: steel reinforced concrete (SRC); T-shaped column; damage evolution; damage model; experimental study; various loadings

1. Introduction

Special-shaped column structure is a kind of structure with special-shaped columns instead of traditional rectangular columns as load-bearing columns. The cross sections of the special-shaped column are mainly L-shaped, T-shaped, Z-shaped or \perp -shaped. The width of the special-shaped column is equal to the infilled walls, which makes a better use of available space, and improves the aesthetic appearance of structures. Therefore, it is a kind of structure that conforms to the development demand and trend of modern civil buildings.

From the 1970s, researchers began to study the mechanical performance of reinforced concrete (RC) special-shaped column, especially the calculation of the biaxial eccentric compression bearing capacity (Ramamurthy and Khan 1983, Sinha 1996, Balaji and Murty 2001). From the 1980s, Chinese researchers began to study the RC special-shaped column, beam-column joint and monolithic structure, and carried out tests and theoretical analyses (Cao *et al.* 2005, Wang *et al.* 2010, Xiao *et al.* 2002). Due to the advantages of special-shaped column structure, good economic and social benefits were

achieved after this kind of structure was put into practical application. However, with the advancement of practical application and scientific research, some disadvantages of RC special-shaped column structure were gradually exposed, such as low bearing capacity and weak seismic performance (Anzlin *et al.* 2015, Kawakami *et al.* 1985, Landi *et al.* 2015), which hindered the development of special-shaped column structure. In 2008, the earthquake in Wenchuan brought great losses to the people's lives and property. Earthquake damage investigation again shows that it is important to improve the seismic performance of such buildings (Yuan 2008). In order to further expand the application of the special-shaped column structure, especially in high intensity earthquake regions, it is an urgent problem to improve the bearing capacity and seismic performance of RC special-shaped column structure.

Steel reinforced concrete (SRC) with special-shaped column is a new type of column formed by configuring shape steel in the section of RC special-shaped column. It not only retains a lot of advantages of the RC special-shaped column, but also inherits the advantages of SRC column, such as high bearing capacity and good seismic performance. Through exploration and practice, it is shown that the SRC special-shaped column can overcome the shortcomings of the RC special-shaped column and expand the application of special-shaped column structure. At present, lots of researchers have carried out researches on the mechanical performance of SRC special-shaped column structure. For SRC special-shaped column, Tokgoz and Dunder (2012) carried out eccentric compression tests on

*Corresponding author, Ph.D.,
E-mail: jiayang_xue@163.com

^a Ph.D. Candidate, E-mail: zhouchaofeng163@163.com

^b Associate Professor, Ph.D.,
E-mail: liuzuqiang0081@126.com

SRC L-shaped columns. Song *et al.* (2007) undertook eccentric compression tests on SRC special-shaped columns, and developed a numerical procedure for the bearing capacity of normal section. Xu *et al.* (2007, 2009) performed the axial compression and eccentric compression experiment on solid-web SRC special-shaped columns, and obtained their failure models under different pressure conditions. Li *et al.* (2007) studied the shear behavior of lattice SRC special-shaped columns, and analyzed the influence of different parameters on shear capacity and ductility. Chen *et al.* (2005, 2007, 2016) presented an experimental study on SRC special-shaped columns under low cyclic reversed loading, and obtained their seismic performance indices and axial compression ratio limit values. Xue *et al.* (2012) took an experimental study on SRC special-shaped columns and proposed the calculation method about the bearing capacity. For SRC special-shaped column-RC beam joints, Deng *et al.* (2010) conducted an experimental study on side joints of SRC frame with special-shaped columns under low cyclic reversed loading. Xue *et al.* (2009, 2011) carried out an experimental study on corner joints, side joints and middle nodes located in the SRC special-shaped column frame, and analyzed their seismic performance indices under low cyclic reversed loading. Chen *et al.* (2014) presented an experimental study on plane and spatial joints, and analyzed their hysteretic behaviors. For SRC frame with special-shaped columns, Yang *et al.* (2015) presented a quasi-static experimental study on a one-bay and two-story plane frame with 1/2 scale which consisted of RC beams and SRC T-shaped columns. Xue *et al.* (2014) and Liu *et al.* (2014) performed an experimental study on three 1/2.5-scaled plane frames with two-bay and three-story under low cyclic reversed loading, and made some insights into the monolithic seismic performance of the SRC frame with special-shaped columns.

As a new type of structure, many scholars had conducted experimental researches on SRC special-shaped columns, column-beam joints and plane frames with special-shaped columns under low cycle reversed loading. However, the damage evaluation criterion and damage model for SRC special-shaped columns have not been established and further studies of damage mechanism of this structural system is needed. As well known, earthquake will cause structural damage, which leads to the deterioration of building material properties, bearing capacity and stiffness. When the damage reaches a certain extent, the structure will be unable to bear vertical load and a whole or local collapse will happen to structure. Therefore, it is necessary to establish a damage model based on component, so as to achieve local damage assessment and monolithic damage assessment, to achieve the purpose of catastrophic control under earthquake (Krawinkler and Zohrei 1983, Mehanny and Deierlein 2001, Shin *et al.* 2014, Kamaris *et al.* 2012, 2016). Earthquake damage investigation shows that structural damage is caused by deformation and cyclic cumulative energy dissipation. The single-parameter model based on energy dissipation or deformation is not very accurate, while the dual-parameter model based on deformation and energy is relatively more accurate. The

most representative dual-parameter model is the Park-Ang model, which is proposed based on the linear combination of maximum deformation and cumulative hysteretic energy (Park and Ang 1985a, b). The Park-Ang model, a dual-parameter damage model based on RC column and beam tests, provides a useful reference for the analysis of structural damage. However, the Park-Ang model can't accurately reflect the damage evolution laws of SRC special-shaped column.

In order to fill the gap of the research on the damage of SRC special-shaped column, ten SRC T-shaped columns with different steel ratios and axial compression ratios were designed and examined the damage mechanism under different loading modes. Considering the effect of energy and deformation, a dual-parameter damage model is proposed for the SRC T-shaped columns in this paper. The damage index is adopted to assess the damage degree of such components in each damage stage. Meanwhile, this research enriches the theory of SRC special-shaped column structure, and expands the application of special-shaped column structure, especially in high seismic intensity areas, which has a very important theoretical significance and engineering practical value.

2. Experimental program

2.1 Specimen design

A total of ten solid-web SRC T-shaped columns were designed with a scale ratio of 1/2 and a shear span ratio of 2.5. The specimens had a prototype of a T-shaped column with a sectional depth-thickness ratio of 3, and the limb thickness of 240 mm. The loading was applied along the web. In order to consider the effects of the different parameters on the damage of the SRC T-shaped columns, the steel ratio, the axial compression ratio and the loading mode were taken as variables. The section size and shape steel configuration are shown in Fig. 1. The design parameters are shown in Table 1, where n is the axial compression ratio, ρ_s is the longitudinal reinforcement ratio in the column cross section, ρ_{ss} is the shape steel ratio in the column cross section.

Table 1 Experimental parameters

Specimen ID	n	$\rho_s/\%$	$\rho_{ss}/\%$	Loading mode
T1	0.4	0.873	7.09	monotonic loading
T2	0.4	0.873	7.09	hybrid loading
T3	0.4	0.873	7.09	hybrid loading
T4	0.4	0.873	7.09	hybrid loading
T5	0.4	0.873	7.09	constant amplitude cyclic loading
T6	0.4	0.873	7.09	variable amplitude cyclic loading
T7	0.2	0.873	7.09	variable amplitude cyclic loading
T8	0.6	0.873	7.09	variable amplitude cyclic loading
T9	0.4	0.873	6.18	variable amplitude cyclic loading
T10	0.4	0.873	8.01	variable amplitude cyclic loading

Table 2 Mechanical properties of steel plates and reinforced bars

Steel form	Thickness/diameter $t(R)/\text{mm}$	Yield strength f_y/MPa	Yield strain $\epsilon_y/10^{-6}$	Ultimate strength f_u/MPa	Ultimate strain $\epsilon_u/10^{-6}$	Elasticity modulus E_s/MPa	Elongation $\delta/\%$
Steel plate	5	321.0	1507	475.1	2231	2.13×10^5	31.3
	8	306.8	1590	468.9	2430	1.93×10^5	28.6
	12	298.5	1415	432.2	2048	2.11×10^5	26.3
	16	285.0	1397	445.6	2184	2.04×10^5	30.2
	20	279.6	1405	412.7	2074	1.99×10^5	23.5
	24	269.3	1360	407.2	2057	1.98×10^5	23.7
Rebar	6	391.9	1866	587.6	2798	2.10×10^5	27.5
	10	369.0	1757	518.7	2470	2.10×10^5	28.3

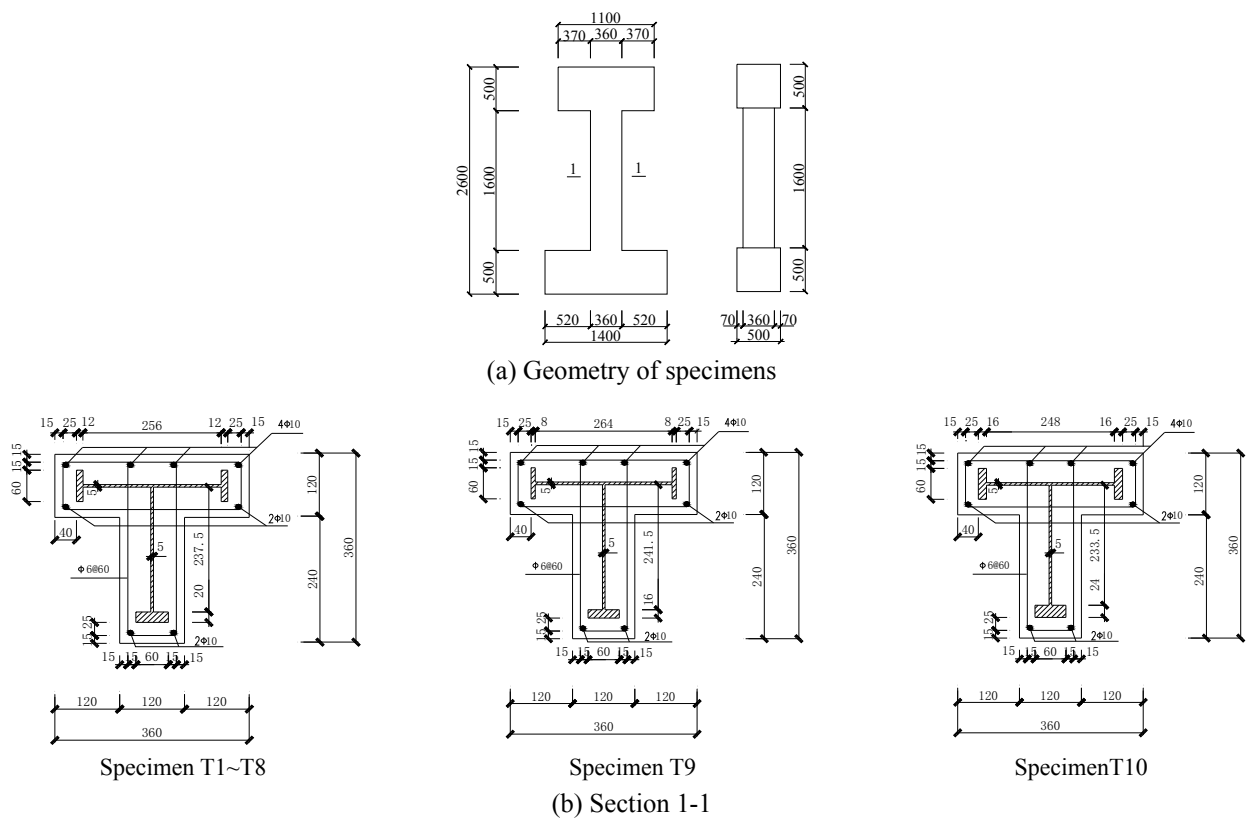


Fig. 1 Geometry and steel details of specimens

The concrete design strength grade was C30. During the process of specimen casting, concrete cubic blocks were reserved. The compression strength of the cube was measured as 34.5 MPa. Q235B was used for shape steel, with HPB300 for longitudinal rebar and stirrup. The mechanical properties are shown in Table 2.

2.2 Loading device and loading mode

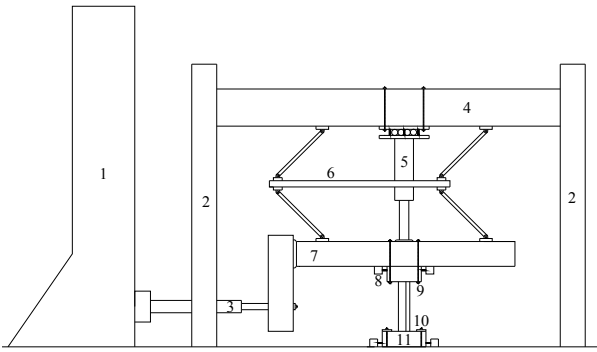
2.2.1 Loading device

The test was carried out in the civil engineering laboratory of Xi'an University of Architecture and Technology. The PCE loading device (PCE is a Japanese device used in pseudo-static tests on structures) was used, as shown in Fig. 2. Prior to the loading process, a hydraulic

jack was adopted to impose constant axial gravity load. Then, a horizontal MTS electro-hydraulic servo actuator was applied to impose monotonic or low cyclic reversed loading.

2.2.2 Loading modes

In order to examine the effects of the different loading modes on the damage of the SRC T-shaped column, four loading modes were used for testing specimens. Before component yielding, the force-control was used with a per level load increment of 20 kN. When the horizontal load-displacement curve appeared obvious inflection point and the strain of the steel in column base exceeded the yield strain of the steel, it was considered that the specimen entered into the yield stage. After yielding, the displac-



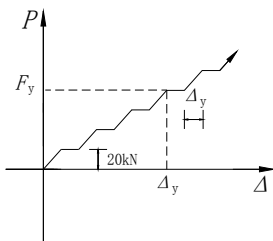
1 reaction wall. 2 reaction steel frame.
 3 MTS electro-hydraulic servo actuator. 4 reaction girder.
 5 hydraulic jack. 6 parallel four-connecting rods.
 7 L-shaped translational steel beams. 8 square steel tube.
 9 high strength bolts. 10 rigid compression beams.
 11 specimen

(a) Schematic diagram of PCE loading device

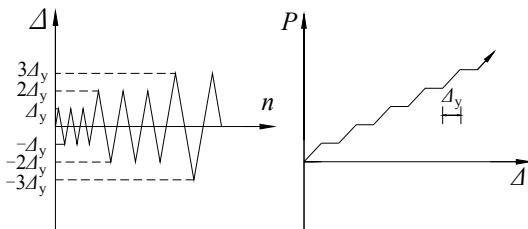


(b) Picture of actual PCE loading device

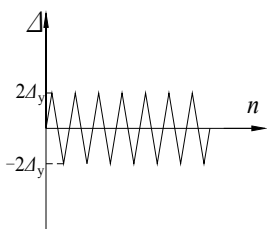
Fig. 2 Test setup



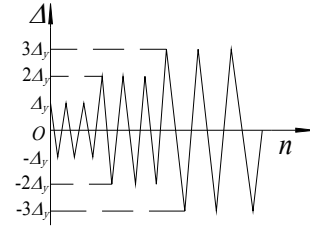
(a) Monotonic loading



(b) Hybrid loading



(c) Constant amplitude cyclic loading



(d) Variable amplitude cyclic loading

Fig. 3 Loading history of specimens

ment-control was used with a per level displacement amplitude as the multiple of yield displacement, and loading ceased until the bearing capacity fell to 85% of the peak load. The specific loading modes are as follows:

- (i) A monotonic loading was used for specimen T1, as shown in Fig. 3(a).
- (ii) A hybrid loading mode was used for specimen T2, T3, and T4. Prior to yielding, horizontal force imposed using the force-control scheme was reversed only once at each control point. After yielding, it was reversed three times at each control point. When it was loaded to $1\Delta_y$, $2\Delta_y$, and $3\Delta_y$ (Δ_y is yield displacement) respectively, the monotonic loading was carried out for specimens, as shown in Fig. 3(b).
- (iii) A constant amplitude cyclic loading was used for specimen T5, with the displacement amplitude of $2\Delta_y$, as shown in Fig. 3(c).
- (iv) A variable amplitude cyclic loading was used for specimen T6~T10. Prior to yielding, per level loading was repeated once, while after yielding, per level displacement cycled three times, as shown in Fig. 3(d).

2.3 Measurement points layout

The measurement points are distributed as illustrated in Fig. 4. The main test contents included horizontal displacement, rebar strain and shape steel strain. The displacements on top of the specimen, inflection point and column base were measured by displacement transducers. The strain responses were measured by strain gages in the loading process, and strain gage A~H and strain gage 1~12 represented rebar strain and shape steel strain, respectively.

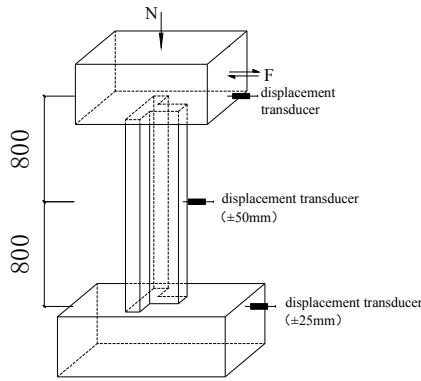
3. Test results analysis

3.1 Failure process of specimens

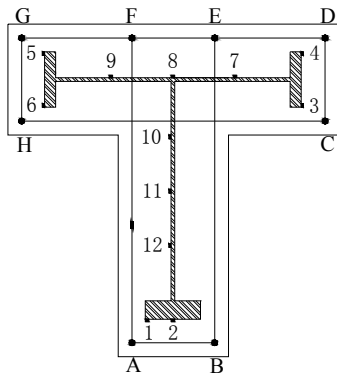
In order to describe the test phenomenon concisely, the SRC T-shaped column surface is marked as shown in Fig. 5. The load was positive as push, negative as pull. The damage process of the specimens could be divided into five stages, namely non-damage, slight-damage, steadily-developing-damage, severe-damage, and complete-damage.

3.1.1 Monotonic loading

For specimen T1, when the horizontal load increased to



(a) Displacement measuring point



(b) Strain measuring point

Fig. 4 Measuring points layout

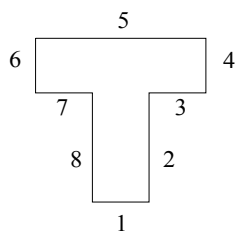


Fig. 5 The specimen surface number

60 kN, no cracks appeared on the surface of the specimen, and the specimen was in the non-damage stage. When the load was added to 80 kN, horizontal cracks appeared at the column base of surface 1 and 8. When the load reached 120 kN, the horizontal cracks connected, and vertical discontinuous short cracks about 5 cm appeared on both sides of the web, indicating the slight-damage degree for specimen T1. With the increase of the load, the damage was steadily further developed, and concrete spalling occurred at the column base. When the load was increased to 200 kN, the specimen yielded. Furthermore with the increase of the displacement, a large number of horizontal connected cracks and oblique cracks appeared in the tension zones at the top and bottom of the column. When the displacement reached $+3\Delta_y$ (Δ_y is the yield displacement), the concrete on surface 1 was crushed at the column base, and concrete spalling occurred in other surfaces. When the displacement reached $+8\Delta_y$, the concrete at the top and bottom of the

column was subjected to severe damage, accompanied by the yield of longitudinal rebar and stirrup exposure, which indicated severe damage for specimen T1. Following this, with the increase of the displacement, specimen T1 tilted obviously, and the concrete on both the up and down ends were completely crushed and out of function, most of the shape steel was exposed at this point, which indicated that specimen T1 was in the complete-damage stage.

3.1.2 Hybrid loading

Specimen T2, T3, and T4 were tested under hybrid loading. When the horizontal load reached 60 kN~80 kN, fine cracks appeared on both sides of the web. When the load reached 100 kN~120 kN, the horizontal cracks became connected at the column top. Meanwhile, when the load was 120 kN, vertical cracks appeared on both sides of the web, and the specimen was in the slight-damage stage. With the increase of the load, the cracks developed rapidly, and the specimen was in the state of steadily-developing damage. New horizontal cracks constantly appeared along the height of the column. When the load reached 160 kN, a large number of connected cracks occurred at the column top and bottom, which developed obliquely. When the horizontal load was close to 200 kN, all the specimens entered the yield stage. When the horizontal displacement reached $2\Delta_y$, concrete spalling occurred at the top and bottom of column on surface 1 and 5. When the load was $3\Delta_y$, the concrete became crushed at these positions. When the displacement reached $6\Delta_y$, the longitudinal reinforcement and stirrup were exposed, which indicated severe damage for the specimens. When the horizontal displacement reached $9\Delta_y$, a large area of concrete at column bottom was crushed on surface 8, 1, and 2 of specimen T2, the stirrup of specimen T3 was exposed in a large area, and the shape steel were exposed at the base of specimen T4. All of the specimens at this moment entered the complete-damage stage.

3.1.3 Constant amplitude cyclic loading

For specimen T5, when the horizontal load was increased to 60 kN, no cracks occurred on the surface of specimen T5, indicating the non-damage stage of specimen T5. When the load was increased to 80 kN, horizontal fine cracks appeared around the web, indicating slight damage for the specimen. With the increase of the load, new cracks constantly appeared in different parts of specimen. When the load was increased to 100 kN, cracks at the column top became connected on surface 1, and extended to both sides. When the load was increased to 140 kN, horizontal cracks appeared in all of the surfaces at top of the column, and horizontal inclined cracks appeared on surface 8. When the horizontal displacement reached $2\Delta_y$ for the first time, concrete spalling occurred at the column base on surface 1. When the horizontal displacement reached $+2\Delta_y$ for the sixth time, serious concrete spalling appeared at the column base. When the horizontal displacement reached $+2\Delta_y$ for the ninth time, a large area of concrete collapsed, with exposed reinforcement at the intersection of the column base on surface 1 and 8, which indicated the severe damage for specimen T5. In the subsequent reciprocating loading, due to the gradual increase of the specimen cumulative

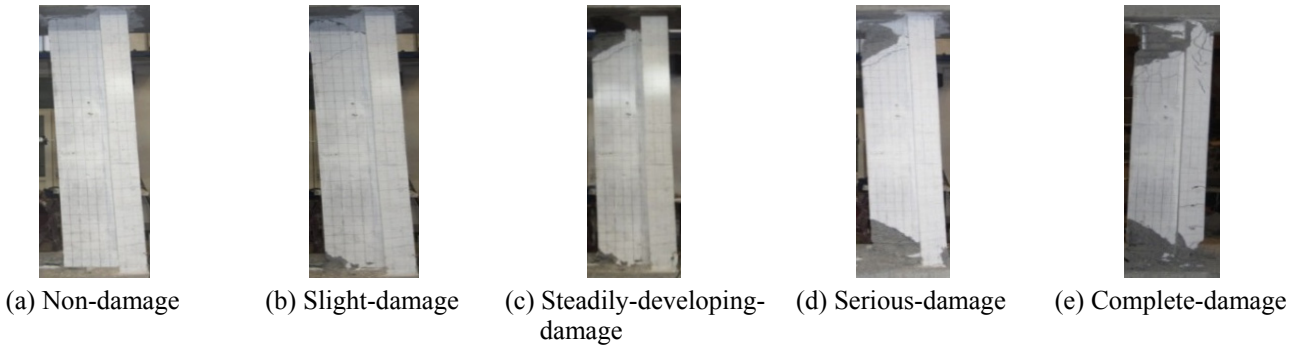


Fig. 6 Damage development of the specimen

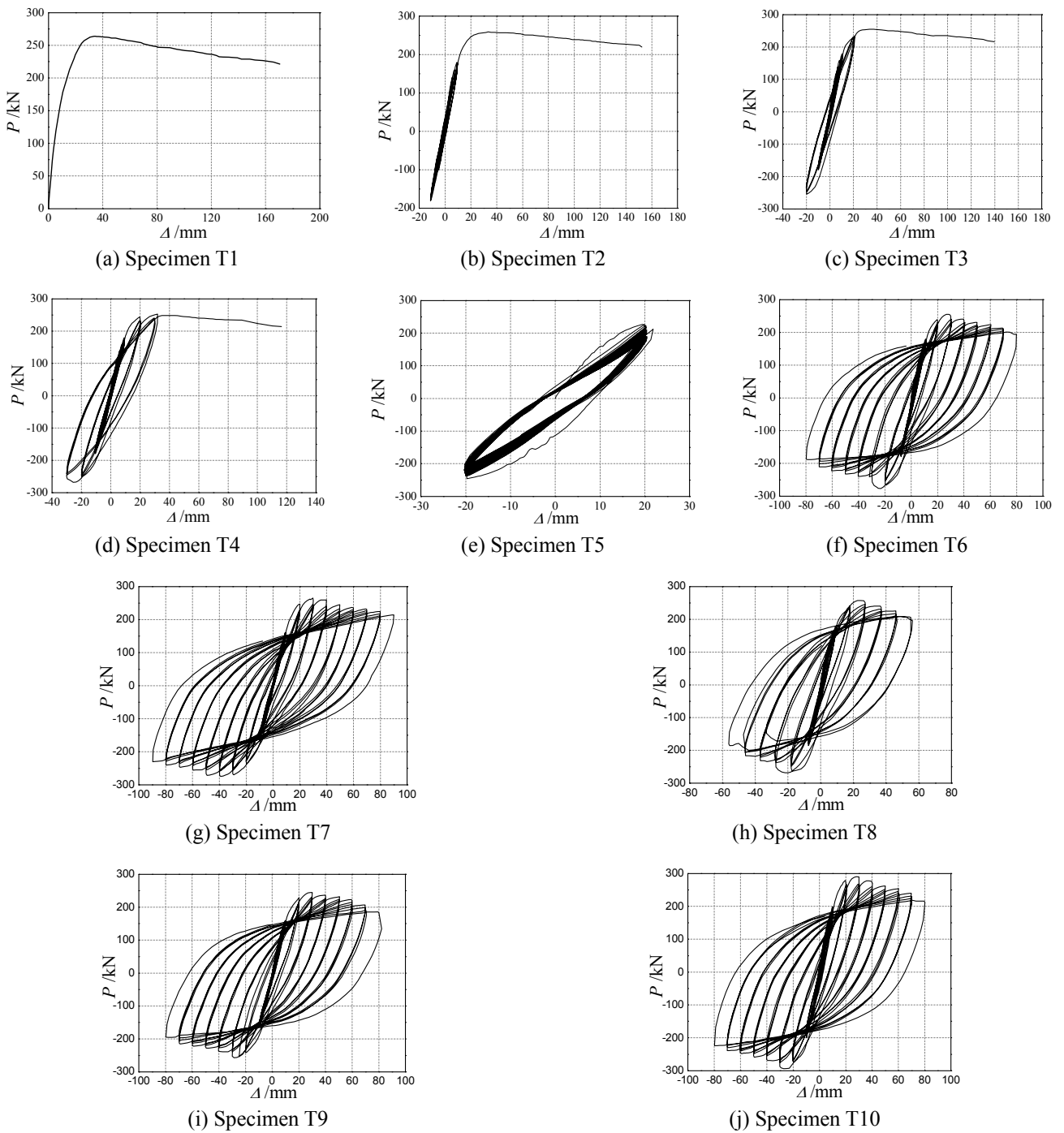


Fig. 7 Load-displacement curves of specimens

damage, the concrete at the top and bottom of the column was gradually crushed. When the horizontal displacement reached $-2\Delta_y$ at the 33rd time, the mass concrete was crushed at the column bottom of surface 2, and the shape steel was exposed at the column base. Finally, when the reversed loading was applied on the specimen for 244 times, specimen T5 was in the complete-damage stage.

3.1.4 Variable amplitude cyclic loading

Specimens T6, T7, T8, T9, and T10 were tested under variable amplitude cyclic loading. When the horizontal load of specimen T7 reached 60 kN, there were some cracks on the surface of specimen T7, and the rest of the specimen experienced cracking at 80 kN. At the initial loading stage, no cracks appeared on the surface, which indicated that the specimens were in the non-damage stage. In the subsequent loading process, the cracks of specimen T7 were found to develop faster than those of the others, and new fine inclined cracks constantly occurred on both sides of the web, which indicated the slight damage degree of the specimens. With the increase of the load, a few of horizontal cracks became connected and a large number of new cracks appeared. When the load reached 200 kN, yield occurred to specimens T6, T7, T8, and T9. Specimen T10 experienced yield at 220 kN. After all of the specimens reached yield, the horizontal cracks developed rapidly and the inclined cracks grew slowly. The mass horizontal cracks became connected on surface 8, 1, and 2 of each specimen, which indicated the stage of serious damage. Compared with the other four specimens, specimen T8 was found to have an obvious failure phenomenon. The damage development process of specimen T8 is shown in Fig. 6. When the displacement reached $2\Delta_y$, a small amount of concrete at the column base was crushed, and concrete spalling occurred at column top. When the displacement increased to $3\Delta_y$, all of the specimens entered into the stage of serious damage. When the horizontal displacement reached $4\Delta_y$, the longitudinal reinforcement was exposed on both sides of the column bottom web for specimen T9. All of the concrete became crushed at the flange of the column bottom and top, as well as the web of specimen T8. Only a small amount of concrete became crushed for specimen T6, T7, and T10. With the increase of the displacement, the specimens gradually entered into the stage of complete damage. In the case of $5\Delta_y$, the longitudinal reinforcement was exposed at the web of the column top for specimen T8, and the shape steel was exposed at the base of specimen T9. Then, the bearing capacity was significantly reduced until complete damage occurred. In the case of $6\Delta_y$, the shape steel was exposed for specimen T6, T7, and T10. A large area of concrete collapsed at the column base. The same situation occurred in the flange at the top of the column for specimen T6.

All specimens showed the bending failure characteristics. Prior to the complete damage for all specimens, a plastic hinge occurred at the column top and bottom, with strong capacities of deformation and energy dissipation. All specimens had smaller shear deformation until the complete damage occurred. Additionally, no stirrup yield was observed.

3.2 Load-displacement curve

The horizontal load-displacement curves are shown in Fig. 7, which indicates the following:

- (i) With the exception of specimen T1, the hysteretic curves of other specimens are basically symmetrical. This is because the constraint boundary condition of the column ends was consistent with the actual situation in the condition that the PCE loading device was used. Also, the inflection point was basically located in the specimen span. In the process of reversed loading, the top and bottom flanges and the web of the specimen alternately underwent tension and compression, and the bearing capacity was the same at the column bottom and top, which led to symmetry hysteretic curves.
- (ii) Specimen T1 with monotonic loading is characterized by high bearing capacity, good ductility, and large displacement at failure. However, when the displacement was added to $1\Delta_y$, $2\Delta_y$, and $3\Delta_y$ for specimen T2, T3, and T4, due to the increase of the cumulative damage, the peak loads and failure displacements of all specimens displayed varying degrees of reduction.
- (iii) Prior to cracking, the curves of all specimens are close to a straight line, and no residual deformation appears after unloading. However, after cracking, the curves are slightly tilted. With the increase of the load, the stiffness degradation of specimens is accelerated. The curves are significantly tilted towards the displacement axis, and the area surrounded by hysteretic curve increases rapidly. In particular, following the peak load, due to the existence of the shape steel and the restriction between the shape steel and the stirrup, the core concrete is still not in the complete damage stage, and the hysteretic curves are shaped as a plump spindle. Prior to the complete damage for all specimens, no obvious "pinching" phenomenon appears, and no obvious bonded cracks are found during the test, which proves that the concrete and shape steel are able to work together.
- (iv) Among the three cycles in the same displacement amplitude, both the bearing capacity and energy consumption performance are reduced in the latter two cycles, and stiffness degradation also appears, which indicates the existence of the cumulative damage. For specimen T5, with the constant amplitude cyclic loading, the degradation rate of the stiffness and the bearing capacity are small. In the later loading, the bearing capacity decreases rapidly owing to the failure of concrete.
- (v) Due to the existence of shape steel, following the peak load, the hysteretic curves fall quite gently. For specimen T8, with a high axial compression ratio, the attenuation rate of bearing capacity is significantly greater than that of other specimens, and the number of loading cycle is less to reach the complete damage stage. With the exception of the

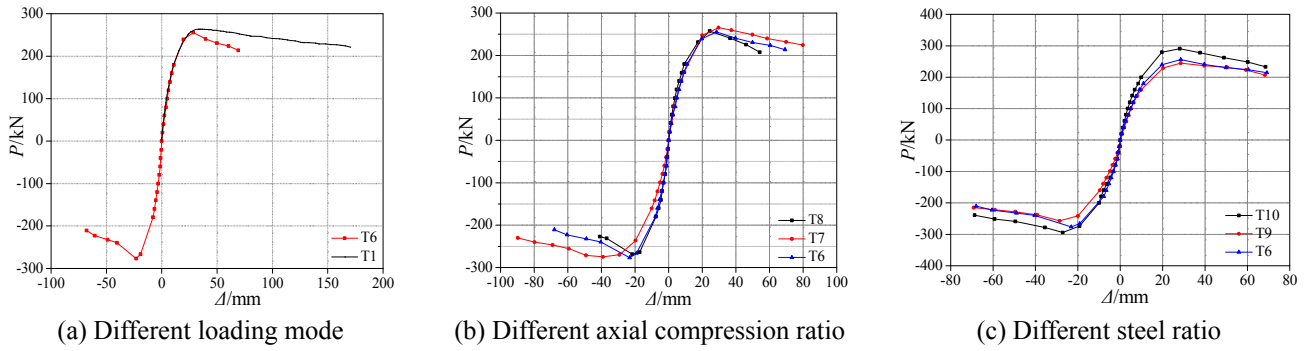


Fig. 8 Envelopes of hysteretic curves of specimens

Table 3 Experimental results of specimens in the main stages

Specimen ID	Loading direction	P_{cr}/kN	Δ_{cr}/mm	P_y/kN	Δ_y/mm	P_m/kN	Δ_m/mm	P_u/kN	Δ_u/mm
T1	Positive	80.00	3.14	200.06	13.72	263.71	33.50	224.15	168.86
	Negative	—	—	—	—	—	—	—	—
T2	Positive	80.00	2.80	198.88	12.81	258.99	33.49	220.14	151.82
	Negative	60.00	2.64	—	—	—	—	—	—
T3	Positive	80.00	2.89	197.98	12.13	254.76	35.32	216.55	137.56
	Negative	60.00	2.32	—	—	—	—	—	—
T4	Positive	80.00	2.70	196.15	12.01	248.68	38.65	211.38	121.19
	Negative	80.00	3.55	—	—	—	—	—	—
T5	Positive	80.00	3.95	—	—	239.41	20.00	—	—
	Negative	—	—	—	—	253.84	20.00	—	—
T6	Positive	80.00	3.91	201.50	14.18	255.52	28.55	217.19	65.79
	Negative	80.00	2.16	197.80	10.29	276.62	19.11	235.13	45.71
T7	Positive	60.00	2.60	207.04	15.01	265.70	29.66	225.85	77.56
	Negative	60.00	2.48	205.50	15.90	274.84	39.04	233.61	85.91
T8	Positive	60.00	1.93	198.50	12.31	257.51	24.50	218.88	51.38
	Negative	80.00	2.13	201.60	9.71	268.77	19.82	228.45	36.54
T9	Positive	80.00	3.91	197.50	14.54	244.59	28.58	207.90	67.56
	Negative	60.00	2.36	191.60	14.72	257.21	28.59	218.63	64.63
T10	Positive	80.00	2.73	226.70	13.66	290.15	28.09	246.63	64.24
	Negative	60.00	1.47	228.00	13.59	294.32	27.09	250.17	60.70

hysteretic curve of specimen T8 which fluctuates near the complete damage stage, the hysteretic curves of the rest specimens are relatively stable, which indicates strong energy dissipation capability and good seismic performance for the rest specimens.

The envelopes of hysteretic curves of some specimens are shown in Fig. 8, and the characteristics of the specimens in different stages are listed in Table 3, where P_{cr} is the cracking load, P_y is the yield load, P_m is the ultimate load, P_u is the failure load, Δ_{cr} , Δ_y , Δ_m , Δ_u are the corresponding displacement, respectively.

- (i) With the exception of the different loading modes between specimen T1 and T6, the other design parameters are the same. As shown in Fig. 8(a),

prior to the peak load, the development trends of the envelopes of hysteretic curves are consistent for the both specimens and almost overlapped. After the peak load, due to the increase of the number of loading cycle and displacement amplitude, the cumulative damage gradually increases, which results in a steep decline for the envelope of hysteretic curve of specimen T6, as well as severe degradation of bearing capacity and stiffness, poorer hysteretic energy dissipation capacity, and small displacement at failure.

- (ii) Among specimen T6, T7, and T8, with the exception of the different axial compression ratios, the other design parameters are the same. It can be seen from Fig. 8(b) that the peak loads of the specimens are not significantly improved with the

increase of axial compression ratio. Meanwhile, following the peak load, specimen T8, which had a larger axial compression ratio, shows a steep decline for its envelope of hysteretic curve, faster stiffness degradation rate, small displacement at failure, and poor ductility. This was due to the fact that in the late loading stage, the second order effect under the large axial compression ratio was more significant.

- (iii) Among specimen T6, T9, and T10, with the exception of the different steel ratios, the other design parameters are the same. As shown in Fig. 8(c), the larger the steel ratio is, the greater the yield load is. Meanwhile, the bearing capacity is significantly improved with the increase of shape steel ratio of the specimens. For example, specimen T6 has a higher steel ratio than T9 by 0.91%, and the average peak load is increased by nearly 6%. Specimen T10 has a higher steel ratio than T9 by 1.83%, and the average peak load is increased by 9.8%. Additionally, the higher the steel ratio is, the gentler the decline segment of the envelope of hysteretic curve is, and the better the ductility is.

Fig. 9 shows the load-displacement curve of the monotonic re-loading for some of the specimens after different cycles. It can be seen from Fig. 9 that, with the increase of the number of loading cycle, the peak loads of specimen T2, T3, and T4 are lower than that of specimen T1 by 1.8%, 3.4%, and 5.7%, respectively, and the failure displacements are reduced by 10.09%, 18.54%, and 28.23%, respectively.

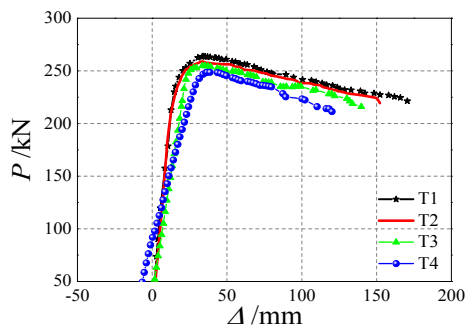


Fig. 9 Monotonic load-displacement curves of specimens after different load cycles

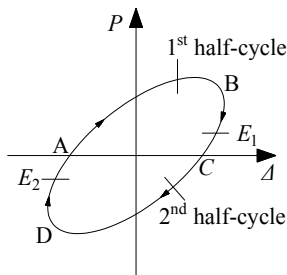
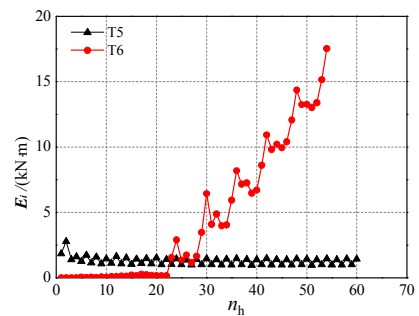


Fig. 10 Definition of half-cycle and hysteretic energy dissipation

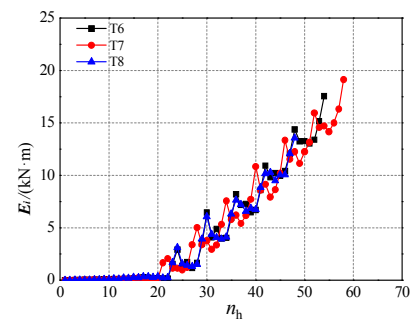
3.3 Energy dissipation analysis

The hysteretic loop generated by a cycle of load or displacement is divided into a positive half-cycle and a negative half-cycle, as shown in Fig. 10, where curve ABC indicates a positive half-cycle, while curve CDA indicates a negative half-cycle. E_1 and E_2 are the hysteretic energy dissipation corresponding to the positive and negative half-cycle, respectively. Fig. 11 shows the relationship between the hysteretic energy dissipation E_i of the i -th half-cycle and the number of half-cycle n_h for the different design parameters.

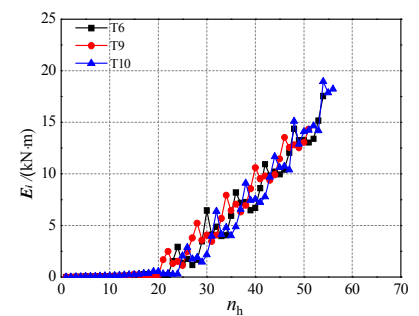
- (i) As illustrated in Fig. 11(a), under constant amplitude cyclic loading, the hysteretic energy dissipation of the positive and negative half-cycle basically remain stable with the increase of the number of half-cycle. But under the variable amplitude cyclic loading, with the increase of the displacement amplitude, the hysteretic energy dissipation of the half-cycle gradually increases. This is because with the increase of the displace-



(a) Different loading mode



(b) Different axial compression ratio



(c) Different steel ratio

Fig. 11 Relationship between hysteretic energy dissipation and the number of half-cycle

ment amplitude, the residual deformation of the specimen increases rapidly, and the damage develops faster under variable amplitude cyclic loading.

- (ii) As shown in Fig. 11(b), at the initial loading stage, the specimens with different axial compression ratios show the same energy dissipation capacities after undergoing the same number of half-cycle. Following the yield of specimen, with the increase of the plastic deformation, the greater the axial compression ratio is, the weaker the energy dissipation capacity of the specimen will be. This is due to the fact that in the cases of a larger axial compression ratio, with the increase of the number of half-cycle, the damage of specimen develops faster.
- (iii) As can be seen in Fig. 11(c), at the initial loading stage, the specimens with different steel ratios also show the same energy dissipation capacities after undergoing the same number of half-cycle. However, when approaching the complete-damage stage at the late loading stage, the larger the steel

ratio of specimen is, the stronger the energy dissipation will be, which leads to a significant increase in energy dissipation. Therefore, increasing the steel ratio of T-shaped column can significantly enhance the energy dissipation capacity of the components, and delay the development of damage.

Fig. 12 illustrates the relationship between the cumulative hysteretic energy dissipation of the specimens ($E = \Sigma E_i$) and the number of half-cycle n_h under the corresponding design parameters.

As can be seen in Fig. 12(a), for specimen T6, the cumulative hysteretic energy dissipation increases sharply after yielding, and the relationship curve between the cumulative energy consumption and the number of half-cycle is close to an exponential function. For specimen T5, under constant amplitude cyclic loading, the relationship curve between the cumulative hysteretic energy dissipation and the number of half-cycle approximates a straight line. At the same time, Fig. 7(e) shows that until specimen T5 enters into the stage of complete damage, the hysteretic energy dissipation of each half-cycle presents no obvious attenuation. Specimen T5 went through 244 times of half-cycles and reached to complete failure. Through the similar relationship shown in Fig. 12(a), the cumulative hysteretic energy dissipation of specimen T5 could be calculated at approximately 300 kN·m at failure, which suggests that under constant amplitude cyclic loading, the total cumulative energy dissipation is very large at failure.

Fig. 12(b) shows that under the same steel ratio, the relationship curve between the cumulative energy dissipation and the number of half-cycle is approximately overlapped for the specimens with different axial compression ratios. These results indicate that the axial compression ratio has smaller influence on the cumulative energy dissipation of the SRC T-shaped column.

Fig. 12(c) proves that the larger the steel ratio of the specimen is, the more slowly the damage develops. Meanwhile, the specimen with a larger steel ratio has a better energy dissipation capacity.

3.4 Strain analysis

In this paper, specimen T6 and T8 are taken as an example to illustrate the strain analysis. Under the horizontal load, the strain of shape steel in column top and column bottom is always greater than the central. The strain response of measuring points near the neutral axis is small and almost in elastic state. So the measuring point (#5 strain gage in Fig. 4(b)) on the flange is selected for analysis, as shown in Fig. 13. At the initial loading stage, the load-strain curves are shaped as a straight line, which indicates that the specimen is in an elastic state with slight damage for shape steel flange. With the increase of the load, the hysteretic curves gradually become plumper. However, strain distribution of the cross section is asymmetric, and the compressive strain is always greater than the tensile strain. These results suggest that, under vertical load and horizontal load, the section strain is unevenly distributed, and the cross section is in an alternated tensile and

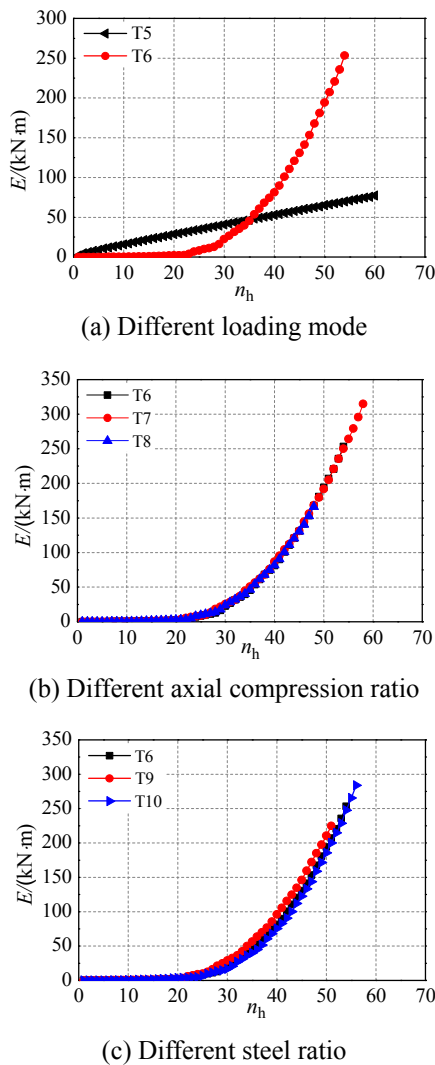
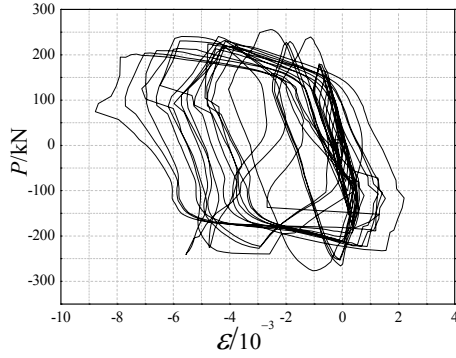
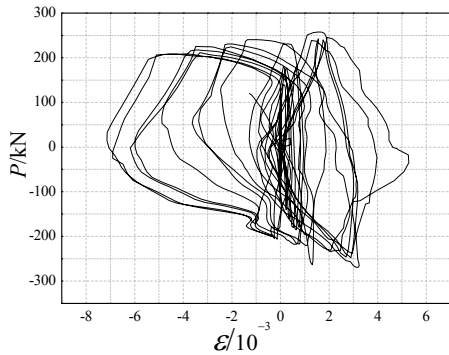


Fig. 12 Relation between cumulative energy dissipation and the number of half-cycle



(a) Specimen T6



(b) Specimen T8

Fig. 13 Strain analysis

compressive stress state. Eventually, the strain of shape steel section far exceeds yield strain with the development of plastic deformation.

4. Damage modeling

In order to quantitatively describe the damage degree of a structure or a component, a damage index D is introduced to establish the damage model of this component.

It can be known from the classic damage theory that the damage index D ranges from 0 to 1. When $D = 0$, it corresponds to the non-damage stage; when $D = 1$, it corresponds to the complete-damage stage of the structure or component; when D ranges from 0 to 1, it corresponds to a certain damage stage between the non-damage and complete-damage of the structure or component (Li and Zhao 1994).

4.1 Park-Ang damage model

At present, the Park-Ang damage model is widely used, with a combination of maximum deformation and cumulative energy dissipation based on a large number of reinforced concrete beam and column tests (Park and Ang 1985a, b), of which the expression is shown as

$$D = \frac{\delta_m}{\delta_u} + \frac{\beta}{F_y \delta_u} \int dE \quad (1)$$

When using an ideal elastic-plastic model, Eq. (1) can be expressed in the following form (Shen *et al.* 1997)

$$D = \frac{\delta_m - \delta_y}{\delta_u - \delta_y} + \frac{\beta}{F_y(\delta_u - \delta_y)} \int dE \quad (2)$$

in which δ_m is the maximum deformation of the component under an actual load; δ_u is the ultimate deformation of the component under a monotonic load; δ_y is the yield deformation; F_y is the yield load of the component; $\int dE$ is the cumulative hysteretic energy dissipation; and β is the combination parameter.

The model is derived from a certain assumption based on test results and an energy method. However, the following deficiencies also exist: (i) under the monotonic load, according to Eq. (1) for the calculation, the damage index D is not equal to 1 in the complete damage stage, while the corresponding damage index was 0 in an elastic state; (ii) the Park-Ang model is unable to reflect the influences of different loading modes on the damage of a structure or a component; (iii) the combination parameter value is difficult to determine with high discreteness; (iv) the model is mainly put forward from the reinforced concrete test data, and the components are regular shaped in a section form, which is unable to be directly applied to the SRC special-shaped column structure; (v) the damage model is a simple linear combination of the deformation and energy parameters.

4.2 Damage modeling of the SRC T-shaped column

In order to overcome the deficiency of the Park-Ang model, based on the test results, a modified damage model is established which is suitable for the SRC T-shaped column. For it, the dynamic relationship between the number of load cycle, deformation amplitude, and ultimate bearing capacity, as well as the effect of the loading modes on the damage is considered.

4.2.1 Damage model derivation

To address the foregoing deficiency of the Park-Ang model, a combination parameter β is introduced to establish a nonlinear damage model which is suitable for SRC T-shaped column, with mutual influences of the maximum inelastic deformation and hysteretic energy dissipation, as seen in Eq. (3)

$$D = (1 - \beta)D_\delta + \beta D_E \quad (3)$$

in which D_δ is the contribution of the maximum inelastic deformation to the damage, and D_E is the contribution of the cumulative hysteretic energy dissipation to the damage.

The D_δ and D_E expressions are shown as follows

$$D_\delta = \left(\frac{\delta_{\max} - \delta_y}{\delta_{u,i} - \delta_y} \right)^c \quad (4)$$

$$D_E = \sum_{i=1}^N \left[\frac{E_i}{F_y(\delta_{u,i} - \delta_y)} \right]^c \quad (5)$$

where δ_{\max} is maximum plastic deformation of component in the course of historical loading process; F_y is the yield

load; δ_y is the yield displacement; $\delta_{u,i}$ is the limit deformation of the component during the monotonic loading after the i -th half-cycle; E_i is the hysteretic energy dissipation corresponding to the i -th half-cycle; N is the number of half-cycle during the entire loading process; β is the combination coefficient; and c is the comprehensive impact parameter of the test, related to the constraint form, loading rate, and so on.

Substituting Eqs. (4)-(5) in Eq. (3), the dual-parameter damage model including the relationship between deformation and energy is as follows

$$D = (1 - \beta) \left(\frac{\delta_{\max} - \delta_y}{\delta_{u,i} - \delta_y} \right)^c + \beta \sum_{i=1}^N \left[\frac{E_i}{F_y(\delta_{u,i} - \delta_y)} \right]^c \quad (6)$$

Considering the influences of the number of load cycle on the hysteretic energy dissipation, the hysteretic energy dissipation D_E is further simplified and modified with the following expression

$$D_E = \sum_{i=1}^N \left(\frac{E_i}{E_{u,i}} \right)^c \quad (7)$$

where $E_{u,i}$ is the limit energy dissipation of the component for re-monotonic loading after the i times of the half-cycle loading.

The simplified damage model could be expressed as follows

$$D = (1 - \beta) \left(\frac{\delta_{\max} - \delta_y}{\delta_{u,i} - \delta_y} \right)^c + \beta \sum_{i=1}^N \left(\frac{E_i}{E_{u,i}} \right)^c \quad (8)$$

4.2.2 Model parameter and variable determination

(1) Limited energy dissipation capacity of the component. In order to facilitate the analysis, a normalization process is carried out on the monotonic limited energy dissipation and cyclic cumulative energy dissipation, respectively, as follows

$$\bar{E}_{u,i} = E_{u,i} / E_u \quad (9)$$

$$\alpha = \sum_{k=1}^N E_k / E_u \quad (10)$$

where $\bar{E}_{u,i}$ is the normalized monotonic limit energy dissipation corresponding to the re-monotonic loading after i -th half-cycle; E_u is the limited energy dissipation of the component during the monotonic loading; α is the normalized cyclic cumulative energy dissipation; $\sum_{k=1}^N E_k$ is the cumulative hysteretic energy dissipation of the component during the first k times of the half-cycle loading.

Through fitting the test data in this study, the approximate relationship between $\bar{E}_{u,i}$ and α is obtained, as shown in Fig. 14. The expression is as follows

$$\bar{E}_{u,i} = a + be^{-\alpha/t_1} \quad (11)$$

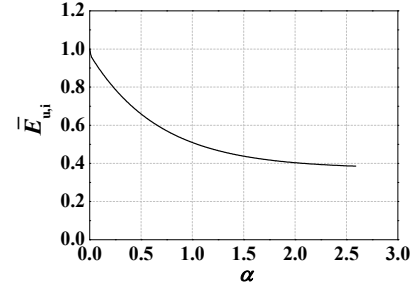


Fig. 14 Relationship of normalized monotonic ultimate energy dissipation and normalized cycle accumulation energy dissipation

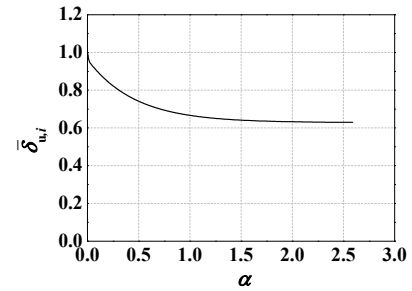


Fig. 15 Relationship of normalized monotonic ultimate displacement and normalized cycle accumulation energy dissipation

in which $a = 0.3723$, $b = 0.6005$, and $t_1 = 0.6773$.

(2) Ultimate deformation capacity of the component. A normalized process is also conducted on the mono-tonic limit deformation as follows

$$\bar{\delta}_{u,i} = \delta_{u,i} / \delta_u \quad (12)$$

in which $\bar{\delta}_{u,i}$ is the normalized monotonic limit deformation corresponding to the re-monotonic loading after i -th half-cycle; δ_u is the failure displacement of the component under the monotonic loading.

The approximate relationship between $\bar{\delta}_{u,i}$ and α is shown in Fig. 15, and the expression is as follows

$$\bar{\delta}_{u,i} = m + de^{-\alpha/t_2} \quad (13)$$

where $m = 0.62846$, $d = 0.33431$, and $t_2 = 0.46195$.

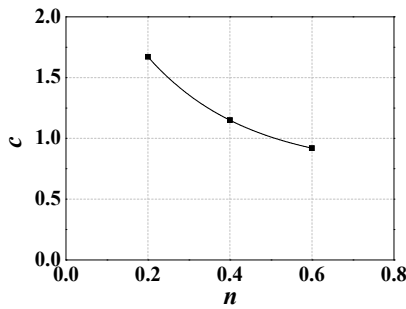
(3) The combination coefficient β and comprehensive influence parameter c .

The experimental results show that, for specimen T5 with a constant amplitude cyclic loading, the attenuation rate of bearing capacity gets smaller, and the cumulative energy dissipation becomes larger. In Eq. (5), the value of D_E gets larger, while the combination coefficient β becomes smaller. Under the variable amplitude cyclic loading, the strength attenuation of the specimens becomes more significant with the increase of the displacement amplitude and the cumulative energy dissipation of these specimens is smaller than that

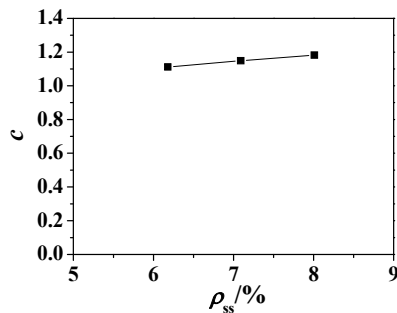
of specimen T5. In Eq. (4), the value of D_δ is larger, and is the same as the combination coefficient β . When compared with the constant amplitude cyclic loading, the variable amplitude cyclic loading is not only closer to the real seismic action, but also reflects the contribution of the deformation to the damage. Also, the $P-\Delta$ curve is able to more intuitively reflect the changes in the mechanical properties of the component. Therefore, when determining the combination coefficient β and test parameter c , only the experimental results under the variable amplitude cyclic loading are analyzed.

The test results (Kumar and Usami 1996) show that it is logical to fix β and evaluate c using variable amplitude cyclic loading test, and the value of β is of order of 0.1~0.2 while c varies between 1 and 2. Therefore, by drawing on the method and referring to the calculation mentioned in (Kumar and Usami 1996), based on test results of T-shaped columns, some trials were carried out on the combination coefficient β . When β equals to 0.12, c has a smaller discreteness. Therefore, in this paper the value of β is chosen as 0.12. Meanwhile, a comprehensive influence parameter c is determined for the SRC T-shaped column with different steel ratios and axial compression ratios, based on the boundary condition of $D = 1$ in the complete-damage stage.

Fig. 16 shows the influences of axial compression and steel ratios on parameter c . It can be seen from Fig. 16 that the parameter c decreases with the increase of the axial compression ratio. An increase of steel ratio leads to a linear



(a) The relation between parameter c and axial compression ratio



(b) The relation between parameter c and steel ratio

Fig. 16 Relationship curves of parameter c and design parameters

Table 4 The calculation of damage index

Specimen ID	n	$\rho_{ss}/\%$	$D_{\text{Modified model}}$	$D_{\text{Park-Ang model}}$
T1	0.4	7.09	1.011	1.103
T2	0.4	7.09	0.991	1.086
T3	0.4	7.09	0.981	1.035
T4	0.4	7.09	0.987	1.069
T6	0.4	7.09	1.044	1.248
T7	0.2	7.09	0.996	1.198
T8	0.6	7.09	1.073	1.298
T9	0.4	6.18	0.987	1.123
T10	0.4	8.01	1.061	1.287

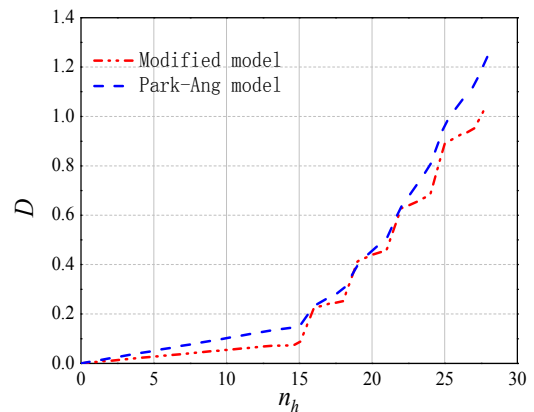


Fig. 17 Comparison analysis of damage index

increase of the parameter c . According to the test design parameters (Table 2), a binary nonlinear regression analysis is carried out on the test parameter c in order to obtain the following expression

$$c = 0.2581 - 0.6971 \ln n + 0.038 \rho_{ss} \quad (14)$$

4.3 Model validation

The modified dual-parameter damage model in this paper and Park-Ang model are respectively used to calculate the damage index of all specimens (except for specimen T5) at failure, and the calculation results are shown in Table 4. It can be seen from Table 4 that the mean damage index of modified model is 1.015 in the complete-damage stage. The standard deviation and the variation coefficient of the modified model are 0.035 and 0.034, respectively. As for Park-Ang model, the mean damage index, the standard deviation and the variation coefficient are 1.160, 0.093 and 0.085, respectively. By comparison, the calculation results of the modified model have a smaller discreteness, and are close to the theoretical upper limit of the damage ("1.0").

A classic Park-Ang model and modified dual-parameter damage model are used to analyze the whole process damage of specimen T6, and the results are shown in Fig. 17. It can be seen from the figure that under the reciprocating loading, when specimen T6 enters the elastic-plastic stage, the damage develops more rapidly with the

development of the plastic deformation. At the same time, compared with the model established in this paper, the classic Park-Ang damage model has a higher calculation value and doesn't accurately assess the damage degree of the SRC T-shaped columns under the same conditions.

5. Conclusions

The damage of solid-web SRC T-shaped columns subjected to various loadings was experimentally investigated. Based on the experimental results, hysteretic behaviour, energy dissipation capacity and the strain of shape steel were analyzed. What's more, a modified nonlinear dual-parameter damage model is proposed. The main conclusions are summarized as follows:

- The hysteretic curves of solid-web SRC column, which were obtained by using the PCE loading device, are plump, symmetric and spindle-shaped, with no "pinching" phenomenon.
- The damage development process of the SRC T-shaped column could be divided into five stages, namely non-damage, slight-damage, steadily-developing-damage, severe-damage, and complete-damage.
- When compared monotonic and re-monotonic loading after multiple cyclic loadings, the decline amplitudes of the bearing capacity and displacement are distributed between 1.78% to 5.70%, and 10.09% to 28.23%, respectively. Also, the energy dissipation ability declines to varying degrees.
- By taking into account of the relationship between the number of loading cycle, displacement amplitude and ultimate resistance, as well as the effect of different loading modes, a nonlinear damage model is established in this paper. A nonlinear relationship between maximum deformation and hysteretic energy dissipation is shown in the damage model mentioned above. Compared with the Park-Ang model, the model proposed in this paper can potentially be used for the damage assessment of SRC T-shaped columns.

Acknowledgments

This work described in this paper was supported by the National Natural Science Foundation of China (Granted No. 51308444), Shaanxi Natural Science Foundation (Granted No. 2014JQ7288) and Innovation Team Project and Youth Technology Fund of Xi'an University of Architecture and Technology (Granted No. QN1408).

References

- Anzlin, A., Fischinger, M. and Isakovic, T. (2015), "Cyclic response of I-shaped bridge columns with substandard transverse reinforcement", *Eng. Struct.*, **99**(9), 642-652.
- Balaji, K.V.G.D. and Murty, D.S.R. (2001), "Reliability analysis of RC T-shaped column sections", *Ind. Concrete J.*, **75**(3), 223-227.
- Cao, W.L., Huang, X.M. and Song, W.Z. (2005), "Experiment and non-linear element analyses of seismic behavior of short specially shaped columns with crossed reinforcing bars", *J. Build. Struct.*, **26**(3), 30-37.
- Chen, Z.P., Zhang, X.D. and Su, Y.S. (2005), "Theoretical research on bearing capacity of normal cross section of SRC special-shaped columns", *Xi'an Univ. Arch. Tech.: Natural Science*, **27**(3), 345-350.
- Chen, Z.P., Xue, J.Y. and Zhao, H.T. (2007), "Experimental study on seismic behavior of steel reinforced concrete special-shaped columns", *J. Build. Struct.*, **28**(3), 53-61.
- Chen, Z.P., Xu, J.J. and Xue, J.Y. (2014), "Experimental investigation on hysteretic behaviour of planar and 3D joints in cruciform SRC column frame", *J. Build. Struct.*, **35**(8), 80-87.
- Chen, Z.P., Xu, J.J. and Chen, Y.L. (2016), "Axial compression ratio limit values for steel reinforced concrete (SRC) special shaped columns", *Steel Compos. Struct., Int. J.*, **20**(2), 295-316.
- Deng, Z.H., Tang, G.X. and Xiang, P. (2010), "Experimental study on seismic behavior of SRC T-shaped column joints under low cyclic reversed loading", *Ind. Constr.*, **40**(6), 44-48.
- Kamaris, G.S., Vallianatou, Y.M. and Beskos, D.E. (2012), "Seismic damage estimation of in-plane regular steel moment resisting and x-braced frames", *Bull. Earthq. Eng.*, **10**(6), 1745-1766.
- Kamaris, G.S., Skalomenos, K.A. and Hatzigeorgiou, G.D. (2016), "Seismic damage estimation of in-plane regular steel/concrete composite moment resisting frames", *Eng. Struct.res*, **115**(5), 67-77.
- Kawakami, M., Tokuda, H. and Kagaya, M. (1985), "Limit states of cracking and ultimate strength of arbitrary concrete sections under biaxial loading", *ACI Struct. J.*, **82**(2), 203-212.
- Krawinkler, H. and Zohrei, M. (1983), "Cumulative damage in steel structures subjected to earthquake ground motions", *Comput. Struct.*, **16**(4), 531-591.
- Kumar, S. and Usami, T. (1996), "Damage evaluation of damage in steel box columns by cyclic loading tests", *J. Struct. Eng., ASCE*, **122**(6), 626-634.
- Landi, L., Conti, F. and Diotallevi, P.P. (2015), "Effectiveness of different distributions of viscous damping coefficients for the seismic retrofit of regular and irregular RC frames", *Eng. Struct.*, **100**(10), 79-93.
- Li, Y.X. and Zhao, S.C. (1994), "Model of cumulative damage in RC and SRC members", *J. Southwest Jiao-Tong Univ.*, **29**(4), 412-417.
- Li, Z., Zhang, X.F. and Guo, Z.Y. (2007), "Experimental study on the mechanical property of steel reinforced concrete short columns of T-shaped cross-section", *China Civil Eng. J.*, **40**(1), 1-5.
- Liu, Z.Q., Xue, J.Y. and Zhao, H.T. (2014), "Cyclic test for solid steel reinforced concrete frames with special-shaped columns", *Earthq. Struct., Int. J.*, **7**(3), 317-331.
- Mehanny, S.S. and Deierlein, G.G. (2001), "Seismic damage and collapse assessment composite moment frames", *J. Struct. Eng., ASCE*, **127**(9), 1045-1053.
- Park, Y.J. and Ang, A.H.S. (1985a), "Mechanistic seismic damage model for reinforced concrete", *J. Struct. Eng., ASCE*, **111**(4), 722-739.
- Park, Y.J. and Ang, A.H.S. (1985b), "Seismic damage analysis of reinforced concrete buildings", *J. Struct. Eng., ASCE*, **111**(4), 740-757.
- Ramamurthy, L.N. and Khan, T.H. (1983), "L-shaped column design for biaxial eccentricity", *J. Struct. Eng.*, **109**(8), 1903-1917.
- Shen, Z.Y., Dong, B. and Cao, W.X. (1997), "Development and evaluation of researches on damage accumulation analysis for building structures", *J. Tong-Ji Univ.*, **25**(2), 135-140.
- Shin, J., Kim, J. and Lee, K. (2014), "Seismic assessment of

- damaged piloti-type RC building subjected to successive earthquakes”, *Earthq. Eng. Struct. Dyn.*, **43**(11), 1603-1619.
- Sinha, S.N. (1996), “Design of cross (+) section of column”, *Ind. Concrete J.*, **70**(3), 153-162.
- Song, H.J., Su, Y.S. and Luo, Y.F. (2007), “Loading-bearing capacity of normal cross section of SRC L-shaped columns”, *J. Tongji Univ. (Natural Science)*, **35**(12), 1597-1601.
- Tokgoz, S. and Dundar, C. (2012), “Tests of eccentrically loaded L-shaped section steel fibre high strength reinforced concrete and composite columns”, *Eng. Struct.*, **38**(5), 134-141.
- Wang, T.C., Zhang, X.H. and Zhao, H.L. (2010), “Experimental research on seismic behavior of exterior joints with specially shaped columns reinforced by fiber”, *Ind. Constr.*, **40**(1), 46-50.
- Xiao, J.Z., Huang, J. and Zhang, J.R. (2002), “Experimental study on seismic behavior of HPC side frame structure with specially-shaped columns”, *J. Build. Struct.*, **23**(6), 19-25.
- Xue, J.Y., Liu, Y. and Zhao, H.T. (2009), “Experimental study on seismic behavior of steel reinforced concrete special-shaped column-beam joints”, *J. Build. Struct.*, **30**(4), 69-77.
- Xue, J.Y., Liu, Y. and Chen, Z.P. (2011), “Experimental study of the bearing capacity of steel reinforced concrete specially-shaped column-beam joint”, *China Civil Eng. J.*, **44**(5), 41-48.
- Xue, J.Y., Chen, Z.P. and Zhao, H.T. (2012), “Shear mechanism and bearing capacity calculation on steel reinforced concrete special-shaped columns”, *Steel Compos. Struct., Int. J.*, **13**(5), 473-487.
- Xue, J.Y., Gao, L. and Liu, Z.Q. (2014), “Experimental study on mechanical performances of lattice steel reinforced concrete inner frame with irregular section columns”, *Steel Compos. Struct., Int. J.*, **16**(3), 253-267.
- Xu, Y.F., Song, B.F. and Li, G. (2007), “Testing of axial pressure bearing capacity of cross-shaped steel reinforced concrete columns”, *J. Shenyang Jianzhu Univ. (Natural Science)*, **23**(6), 910-914.
- Xu, Y.F., Diao, X.Z. and Guo, J. (2009), “Experimental study on the biaxial eccentric pressure bearing capacity of cross-shaped steel reinforced concrete columns”, *J. Shenyang Jianzhu Univ. (Natural Science)*, **25**(1), 100-105.
- Yang, T., Zhang, X.D. and Zhong, H.N. (2015), “Pseudo-dynamic test on seismic behaviour of frame with T-shaped SRC columns”, *J. Central South Univ. (Science and Technology)*, **46**(6), 2171-2177.
- Yuan, F.Y. (2008), “Loss assessment of Wen chuan earthquake”, *J. Earthq. Eng. Eng. Vib.*, **28**(5), 10-19.